INTERNATIONAL JOURNAL FOR NUMERICAL METHODS IN FLUIDS
Int. J. Numer. Meth. Fluids 2003; **43**:1371–1389 (DOI: 10.1002/fld.568)

Verification testing in computational fluid dynamics: an example using Reynolds-averaged Navier–Stokes methods for two-dimensional flow in the near wake of a circular cylinder

Jennifer Richmond-Bryant*,†

MANTECH Environmental Technology, Inc., P.O. Box 12313, Research Triangle Park, NC 27709, U.S.A.

SUMMARY

Verification testing was performed for various Reynolds-averaged Navier–Stokes methods for uniform flow past a circular cylinder at $Re = 5232$. The standard and renormalized group (RNG) versions of the k–ε method were examined, along with the Boussinesq, Speziale and Launder constitutive relationships. Wind tunnel experiments for flow past a circular cylinder were also performed to obtain a comparative data set. Preliminary studies demonstrate poor convergence for the Speziale relationship.

Verification testing with the standard and RNG k–ε models suggests that the simulations exhibit global monotonic convergence for the Boussinesq models. However, the global order of accuracy of the methods was much lower than the expected order of accuracy of 2. For this reason, pointwise convergence ratios and orders of accuracy were computed to show that not all sampling locations had converged (standard k–ε model: 19% failed to converge; RNG k–ε model: 14% failed to converge). When the non-convergent points were removed from consideration, the average orders of accuracy are closer to the expected value (standard k–ε model: 1.41; RNG k–ε model: 1.27). Poor iterative and global grid convergence was found for the RNG k–ε/Launder model. The standard and RNG k–ε models with the Boussinesq relationship were compared with experimental data and yielded results significantly different from the experiments. Copyright © 2003 John Wiley & Sons, Ltd.

KEY WORDS: k–ε methods; circular cylinder; near wake; verification

INTRODUCTION

Stern *et al.* [1] and Roache [2] have established methodologies for testing the accuracy of computational fluid dynamics (CFD) simulations based on the principles of experimental quality assurance techniques. This entails a two-pronged approach: verification and validation. According to AIAA, *verification* is 'the process of determining that a model implementation accurately represents the developer's conceptual description of the model and the solution to

*Correspondence to: Jennifer Richmond-Bryant, MANTECH Environmental Technology, Inc., P.O. Box 12313, Research Triangle Park, NC 27709, U.S.A.
†E-mail: richmond-bryant.jennifer@epa.gov

Received 27 March 2002
Revised 20 March 2003

the model' [3]. Verification ensures that there is little error between the true solution to the equations being solved and the approximate numerical solution. *Validation* is the process of ensuring that a numerical solution is within some error tolerance of either physical results obtained in the laboratory or of an analytic solution. This study focuses upon the verification process and its effect on model interpretation. The case selected for study is the airflow past a circular cylinder at $Re = 5232$ using steady Reynolds-averaged Navier–Stokes (RANS) equations with two variations of the k–ε turbulence model.

It is well known that steady RANS solutions of airflow past bluff bodies have been poorly validated with experimental data [4, 5] and when compared with large eddy simulations (LES). Many reasons exist for these shortcomings, including:

- inability of high Reynolds number turbulence models to capture laminar or transitional boundary layer behaviour [6];
- omission of periodic vortex shedding, where the length scale of turbulent fluctuations modelled with the k–ε method are at the scale of the boundary layer rather than the scale of a shedding vortex [4, 6];
- failure to represent the interaction between Reynolds stresses and the mean flow [4];
- late boundary layer separation [7–10];
- excessive turbulence kinetic energy levels at the upstream stagnation point of the bluff body, leading to underestimation of the near wake size [7–13];
- overprediction of dissipation of turbulence kinetic energy [14–16];
- and, inaccurate turbulence closure approximations [17, 18].

Despite these disadvantages, RANS methods are still commonly used in applied fluid dynamics studies (for example [19–21]). The applicability of CFD predictions is strongly dependent upon the modeller's accuracy requirements. Lasher [22] notes four categories for the ability of CFD simulations to predict experimental results:

(I) the simulation predicts experimental results within 'desired engineering accuracy';
(II) the simulation quantitatively and accurately predicts the effects of changes in initial conditions or geometry despite biases in both the initial and changed simulations;
(III) the simulation qualitatively predicts trends in quantities of interest; and
(IV) the simulation in incapable of predicting trends.

Regardless of the problems cited above, those predictions are all, at minimum, category III. Engineers often need to know time-averaged trends for design considerations, in lieu of detailed instantaneous behaviour that is more costly and time consuming to acquire. Category II and III predictions from steady RANS simulations are still very useful to the engineer for obtaining information about a process. Steady RANS methods are commonly available through commercial CFD software and require much less CPU time than do variants of direct numerical simulations (DNS) for the solution of Navier–Stokes, including time-dependent vortex methods and LESs [23]. Many software packages also allow easy creation of computational meshes; this feature enables accommodation of more complex geometries. Furthermore, the coefficients used in the RANS models are generally considered robust enough to fulfill a wide range of engineering problems [23, 24]. It should be reiterated that this study is not intended to persuade the reader to use steady RANS methods over other types of models for bluff body flows; many other studies address model preference through detailed validation [4, 25–27].

The objective of this work is simply to use a set of simulations to illustrate the various issues involved with attaining a verified solution with a commonly used CFD model.

Without analysis of both the iterative convergence and grid-independence issues, comparisons of model results with experimental data have limited value in real-world applications [1, 2]. For instance, the Majumdar and Rodi [6] study yielded better agreement with experimental data using a coarse mesh simulation than with a fine mesh. Had they increased the density of the mesh further, Majumdar and Rodi [6] may have seen a larger divergence from the experimental data despite more accurate numerics. Hence, the agreement between simulation and experiment for the coarse mesh may have been a coincidence and not a function of the numerics. In this study, we explore these verification issues for the circular cylinder problem. A comparison of the model with experimental data acquired in a wind tunnel study of flow past a circular cylinder at $Re = 5232$ is also provided to illustrate the effect of the verification error on the comparison between the models and the experimental data. Verification will be performed based on the velocity field because this is a primary quantity solved in the RANS simulation; derived quantities such as drag and pressure coefficients will not be considered here. Two different turbulence models, the standard and RNG k–ε models, are studied. Additionally, the RNG k–ε model is run with the Boussinesq and Launder constitutive relationships to assess their effect on verification. Preliminary studies performed with the RNG k–ε model using a Speziale constitutive relationship, as well as meshing and boundary layer issues, are also addressed.

COMPUTATIONAL METHODS

All simulations were performed using either the FIDAP v. 8.0.1 computational fluid dynamics software on an IBM 2GB RAM 933 MHz processor PC or FIDAP v. 8.6.2 on an SGI Origin 2400 with 48–400 MHz MIPS R12000 processors and 24 GB RAM. FIDAP is capable of generating unstructured or mapped meshes. After the mesh has been created, boundary conditions, a turbulence model and solution parameters are designated. Then, the finite-element method is used to develop a system of equations for each degree of freedom for each discretized element. A segregated pressure projection method is employed. This method considerably reduces the necessary computational effort for solving the system of equations [28]. The linear system of equations is solved using the conjugate gradient squared method for the symmetric matrix and the conjugate residual method for the non-symmetrical matrix. Streamline upwinding is used to reduce false numerical diffusion [29]. Streamline upwinding is second-order accurate in the transverse direction, but is first-order accurate along the primary flow direction where advection is the dominant transport mechanism. However, given the dominance of convection over diffusion in the streamwise direction, the additional streamwise diffusion does not have a large impact on the order of accuracy of the method. For this reason, the method is still considered to be very nearly second-order accurate.

Mesh development and refinement

Preliminary studies demonstrated that an unstructured mesh could not be refined in a consistent manner; for this reason, a mapped mesh was used. We developed a semi-circular mesh, as shown in Figure 1(a) (full mesh) and 1(b) (close-up), similar to those of Celik

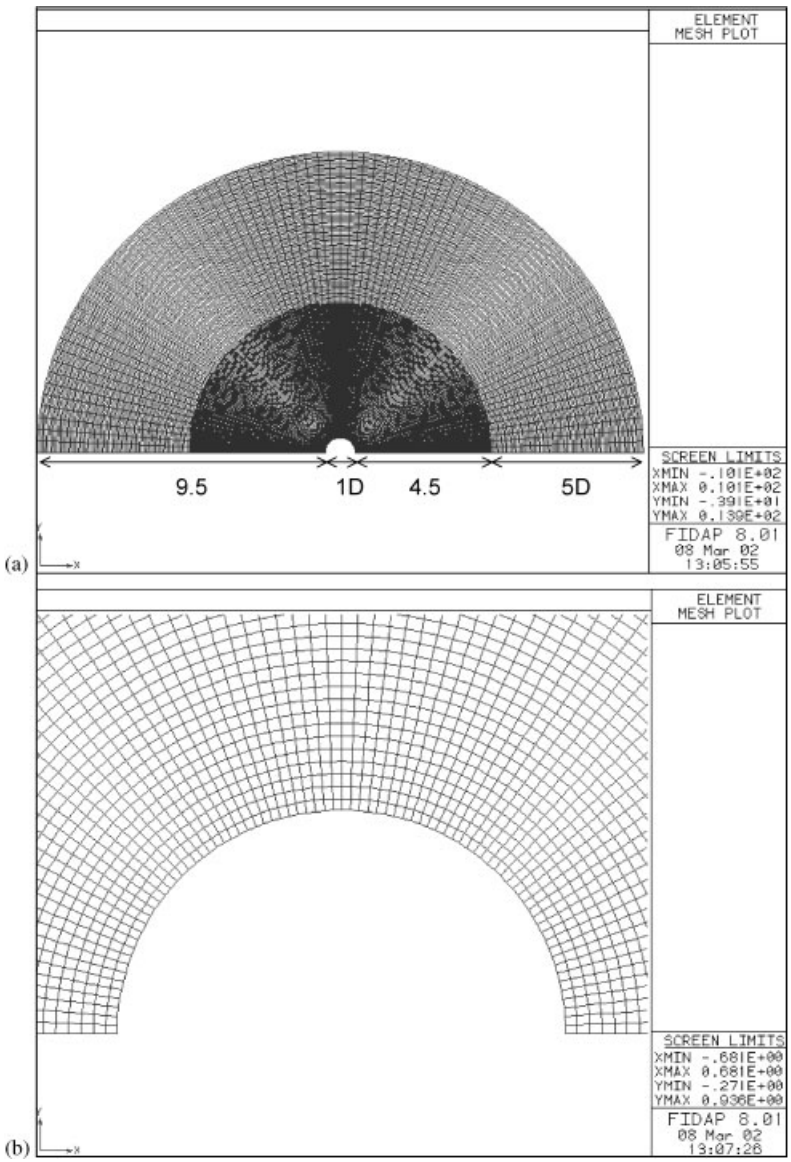

Figure 1. (a) Semi-circular mesh used for the verification and validation studies. (b) Close-up of the mesh near the cylinder boundary.

and Shaffer [30] and Majumdar and Rodi [6]. This mesh is divided into six regions: upstream and downstream outer layers, upstream and downstream inner layers, and upstream and downstream near wall layers, as shown in Figure 1(a). The size of the cell increases radially outward within the inner and outer layers, not including the boundary. The near wall layer is held at a constant thickness with a width of one cell to maintain a consistent

friction velocity profile among the refinements. To conserve computational resources, the inner layers contained twice as many elements as did the outer layers in one-quarter of the space. A mesh refinement factor of $\sqrt{2}$ was applied to the inner and outer layers to determine grid convergence behaviour over three successively finer grids.

Boundary conditions

Boundary conditions were selected to yield the same Reynolds number as the wind tunnel experiments, described below. The simulations were non-dimensionalized by designating $U_\infty = 1$, $D = 1$ and $\rho = 1$. Laminar viscosity was set equal to $1/Re$. Based on the wind tunnel experiments, $Re = 5232$. Inlet kinetic energy was calculated based on the freestream turbulence intensity measured in the tunnel of 3.5%, using $k = 1.5\ (\mathrm{TI} \cdot U_\infty)^2$ to yield a kinetic energy of 1.84×10^{-3} [31].

Based on the relationship between turbulent viscosity, kinetic energy and dissipation, $\mu_t = C_\mu k^2/\varepsilon$, a relationship for ε is derived: $\varepsilon = C_\mu k^2/R_\mu \mu$, where $R_\mu = \mu_t/\mu$ [8, 9, 32]. The term R_μ is used to estimate μ_t for calculation of the inlet value of ε and generally falls in the range $R_\mu = 10$–100. Based on Bosch [33], where he analysed inlet dissipation length scales for wind tunnel experiments performed at $Re = 22,000$ with $\mathrm{TI} = 2\%$ and bluff body blockage of 7%, $R_\mu \sim 10$. These experimental conditions are close enough to the ones used here, $Re = 5232$, $\mathrm{TI} = 3.5\%$, and blockage $= 4.8\%$, to assume $R_\mu = 10$ for the ε boundary condition; this yields an inlet boundary condition of $\varepsilon = 1.59 \times 10^{-4}$. To estimate if the dissipation initial condition is adequate, one can consider that dissipation can be given by $\varepsilon \approx C_\mu k^{3/2}/L$, where $L =$ freestream turbulence length scale. For the honeycomb used as a flow straightener in the experiments, $L = O(0.01\ \mathrm{m})$ and $\varepsilon = O(10^{-4}\ \mathrm{m^2/s^3})$. This is of the same order of magnitude as used in the initial conditions.

Outlet boundary conditions were

$$\frac{\partial u}{\partial n} = 0, \quad \frac{\partial v}{\partial n} = 0, \quad \frac{\partial k}{\partial n} = 0, \quad \frac{\partial \varepsilon}{\partial n} = 0$$

At the cylinder, no-slip conditions apply, and along the symmetry plane, boundary conditions were left free with the exception $v = 0$.

Constitutive relationships

The Reynolds stress term is approximated in FIDAP in one of three ways by linear (Boussinesq), quadratic (Speziale) or cubic (Launder) constitutive relationships. Each of the approximations presented are truncated forms of the true Reynolds stress. For this reason, some error is incurred by the use of any of these formulations [34].

Boussinesq. The Boussinesq constitutive relationship has the linear form

$$-\rho\overline{u_i' u_j'} = 2\mu_t s_{ij} - \tfrac{2}{3} k\delta_{ij} \tag{1}$$

where

$$s_{ij} = \frac{1}{2}\left(\frac{\partial u_i}{\partial x_j} + \frac{\partial u_j}{\partial x_i}\right)$$

and $\delta_{ij} =$ Kronecker delta function.

Speziale. Speziale [35] illustrated that the Boussinesq approximation fails to capture secondary flow structures for the two-dimensional and three-dimensional rectangular fully developed turbulent channel flow problems, and underpredicts the size of the recirculation region for the flow past a backward-facing step. These observations motivated Speziale [35] to develop a second-order Reynolds stress model:

$$-\rho\overline{u_i'u_j'} = 2\mu_t s_{ij} - \frac{2}{3}k\delta_{ij} + 4c_{Sp}c_\mu \frac{k}{\varepsilon}\mu_t \left[s_{il}s_{kj} + \dot{s}_{ij} - \frac{1}{3}(s_{mn}s_{mn} + \dot{s}_{mm})\delta_{ij} \right] \tag{2}$$

where c_{Sp} is a constant (default = 1.68), $\dot{s}_{ij} = -(\partial u_i/\partial x_k)s_{lj} - (\partial u_j/\partial x_k)s_{ki}$, and the subscripts m and n refer to the two unit normals. Speziale [35] found that this second-order constitutive relationship gave better agreement with experimental data for each of the three cases mentioned above.

Launder. Craft *et al.* [36] devised a third-order constitutive relationship. In addition to allowing for secondary eddies and anisotropy, Launder's approximation is intended to better accommodate swirling flows:

$$\begin{aligned}
-\rho\overline{u_i'u_j'} = &-\frac{2}{3}\rho k\delta_{ij} + 2\mu_t s_{ij} + 4c_{L1}\mu_t \frac{k}{\varepsilon}\left(s_{ik}s_{kj} - \frac{1}{3}s_{mn}s_{mn}\delta_{ij} \right) \\
&-4c_{L2}\mu_t \frac{k}{\varepsilon}(\omega_{ik}s_{kj} + \omega_{jk}s_{ki}) - 4c_{L3}\mu_t \frac{k}{\varepsilon}\left(\omega_{ik}\omega_{jk} - \frac{1}{3}\omega_{mn}\omega_{mn}\delta_{ij} \right) \\
&+8c_{L4}c_\mu\mu_t \frac{k^2}{\varepsilon^2}\left(s_{ki}\omega_{lj} + s_{kj}\omega_{li} - \frac{2}{3}s_{km}\omega_{lm}\delta_{ij} \right) s_{kl} \\
&-8c_{L5}c_\mu\mu_t \frac{k^2}{\varepsilon^2}\left(s_{ik}s_{jl} - \frac{1}{3}s_{mk}s_{ml}\delta_{ij} \right) s_{kl} + 8c_{L6}c_\mu\mu_t \frac{k^2}{\varepsilon^2}s_{ij}s_{kl}s_{kl} \\
&-8c_{L7}c_\mu\mu_t \frac{k^2}{\varepsilon^2}s_{ij}\omega_{kl}\omega_{kl}
\end{aligned} \tag{3}$$

The Launder constitutive relationship contains vorticity, ω. Also, note that c_{L1}–c_{L7} are constants (default values: $c_{L1} = 0.1$, $c_{L2} = 0.1$, $c_{L3} = 0.26$, $c_{L4} = 1.0$, $c_{L5} = 0$, $c_{L6} = 0.1$, $c_{L7} = 0.1$), and the subscript l is also used to denote a unit normal.

Turbulence models

Standard k–ε. The standard k–ε model closes the Navier–Stokes equation by providing an estimate for the turbulent viscosity based on the kinetic energy of turbulence, $k = \frac{1}{2}\overline{u_i'u_i'}$, and the viscous dissipation of turbulence kinetic energy, $\varepsilon = (\mu/\rho)(\overline{\partial u_i'}/\partial x_k)(\overline{\partial u_i'}/\partial x_k)$:

$$\mu_t = \frac{C_\mu \rho k^2}{\varepsilon} \tag{4}$$

where C_μ = constant and ρ = fluid density [32].

To obtain u, v, k and ε, a system of equations including the momentum transport equations for u and v and semi-empirical transport equations for k and ε are solved:

$$u_i \frac{\partial k}{\partial x_i} = \frac{1}{\rho} \frac{\partial}{\partial x_i} \left[\left(\mu + \frac{\mu_t}{\sigma_k} \right) \frac{\partial k}{\partial x_i} \right] + \frac{\mu_t}{\rho} (\rho \overline{u_i' u_j'}) \frac{\partial u_i}{\partial x_j} - \varepsilon \tag{5a}$$

$$u_i \frac{\partial \varepsilon}{\partial x_i} = \frac{1}{\rho} \frac{\partial}{\partial x_i} \left[\left(\mu + \frac{\mu_t}{\sigma_\varepsilon} \right) \frac{\partial \varepsilon}{\partial x_i} \right] + \frac{C_1 \mu_t}{\rho} \frac{\varepsilon}{k} (\rho \overline{u_i' u_j'}) \frac{\partial u_i}{\partial x_j} - C_2 \frac{\varepsilon^2}{k} \tag{5b}$$

Equation (5) contains five constants found empirically by Launder *et al.* [37] to apply to a wide range of free turbulent flows: $C_1 = 1.44$, $C_2 = 1.92$, $C_\mu = 0.09$, $\sigma_k = 1.00$ and $\sigma_\varepsilon = 1.30$; these are assumed applicable here. While these constants are generally considered robust, their application might incur some error in the solution given the empirical nature in which they were found.

Renormalized group k–ε. The RNG k–ε model is derived from the RNG theory that smaller scales of multiscale systems, in this case turbulence, can be removed successively through re-scaling to obtain a fixed picture of the system. Details of the method's derivation are given in References [15, 38, 39].

In the RNG k–ε model, the system of Equations (5) is unchanged, with the exception of adding an extra term to the ε-transport equation (5b):

$$-2\nu \left(\frac{\partial u_i}{\partial x_j} + \frac{\partial u_j}{\partial x_i} \right) \frac{\overline{\partial u_l}}{\partial x_i} \frac{\overline{\partial u_l}}{\partial x_j} \approx - \frac{C_\mu \eta^3 (1 - \eta/\eta_0)}{1 + \beta \eta^3} \frac{\bar{\varepsilon}^2}{\bar{k}}$$

where

$$\eta = \left(\frac{\bar{k}}{\bar{\varepsilon}} \right) \sqrt{\frac{1}{2} \left(\frac{\partial \overline{u_i}}{\partial x_j} + \frac{\partial \overline{u_j}}{\partial x_i} \right)^2}$$

the ratio of the characteristic time scale of the turbulent strain to that of the mean flow. Because the RNG k–ε model is derived from theory, rather than from a semi-empirical basis, the coefficients are computed explicitly: $C_1 = 1.42$, $C_2 = 1.68$, $C_\mu = 0.085$ and $\sigma_K = \sigma_\varepsilon = 1.39$ [15, 38].

Near-wall treatment

The FIDAP software uses the Reichardt law to describe boundary layer dynamics. The Reichardt law is a semi-empirical equation for friction velocity [40]:

$$u^+ = \frac{1}{\kappa} \ln(1 + \kappa y^+) + 7.8 \left[1 - \exp\left(-\frac{y^+}{11} \right) - \frac{y^+}{11} \exp(-0.33 y^+) \right] \tag{6a}$$

where y^+ is the non-dimensional distance from the wall, $\kappa \sim 0.41 =$ von Karman constant. Equation (6a) overlaps both the laminar region of the boundary layer ($y^+ < 5$):

$$u^+ = y^+ \tag{6b}$$

and the turbulent boundary layer ($y^+ > 30$):

$$u^+ = \frac{1}{\kappa} \ln(Ey^+) \tag{6c}$$

where E is an empirical constant, $E \sim 9.0$ for smooth walls.

This wall function approach replaces the need for a very fine discretization in the vicinity of a no-slip surface, and it makes simulations with boundaries more feasible, in terms of computational resources. However, this model assumes that turbulence kinetic energy and dissipation are constant throughout the wall elements [28]. This is an unphysical assumption because k and ε should approach zero at a wall boundary. This provides another source of error in the k–ε models.

Although the use of Equations (6a)–(6c) is assumed valid for any y^+, FIDAP [28] recommends that the user maintain $y^+ > 30$ to minimize any errors in the assumption of the Reichardt law. To do so, the cell next to the boundary is kept at a fixed height that is large enough to contain the laminar and transitional regions of the boundary layer. However, this approach has been questioned in Launder [41], Rodi [7], and others because the law of the wall is invalid where flow is separated. Furthermore, Celik and Shaffer [30] argue that, because k and ε are not solved in the boundary layer, that the value of y^+ should be inconsequential. In the FIDAP formulation, a mixing length model using van Driest's formulation is used to find the eddy viscosity in the boundary layer.

To test whether Celik and Shaffer's [30] assertion is true, preliminary studies were run on a coarse mesh of 38 642 elements with an RNG k–ε model and the Boussinesq Reynolds stress approximation. Two simulations were run with boundary layer thicknesses of 0.025 and 0.05. The smaller boundary layer thickness yielded an attached region $y^+ \sim 15$, while the larger boundary layer thickness yielded an attached region $y^+ \sim 30$. A typical y^+ profile around the cylinder is given in Figure 2 for a boundary layer thickness of 0.025. The error between the two simulations varied from 2.1 to 4.6% for u, v, k and ε and was 6.7% for p. For this reason, the smaller boundary layer thickness was used for subsequent runs. This selection was made to preserve a smoother gradient in the mesh near the boundary layer upon mesh refinement outside the boundary layer.

Numerical procedure

Errors in the numerical simulation δ_{SN} can be broken down as a function of contributions from iteration δ_I, meshing δ_M, time step (if unsteady) δ_T and other parameters δ_P [1]:

$$\delta_{SN} = \delta_I + \delta_M + \delta_T + \delta_P \tag{7}$$

In the above analysis, iteration error is first reduced as much as possible. Iteration error is computed as the relative L_2 error norm for a given degree of freedom, X, and must be lower than a user-designated solution error tolerance, ε_τ, for convergence to occur at iteration i [28]:

$$\frac{\|\Delta X_i\|}{\|X\|} < \varepsilon_\tau \tag{8}$$

where $\Delta X_i = X_i - X$. Convergence is achieved in FIDAP when all degrees of freedom, at all nodes, fall beneath ε_τ. Before analysing the grid convergence of each turbulence model, iterative convergence is tested on a coarse grid for each model. To assess the error between

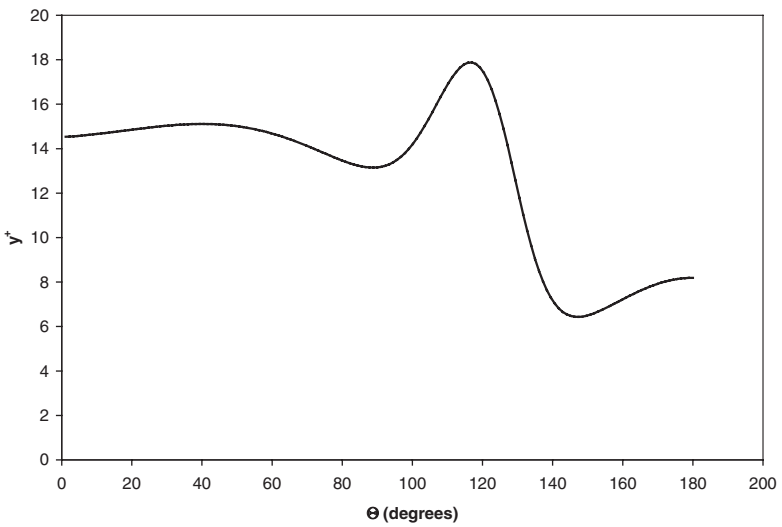

Figure 2. A typical y^+ profile for standard and RNG k–ε models using either the Boussinesq or Launder constitutive relationships.

each level of the solution error tolerance, it is reduced sequentially by an order of magnitude from 10^{-3} to 10^{-6}. The error between each level of tolerance refinement is estimated at 100 locations in the near-wake region over $0 \leqslant y/D \leqslant 0.5$, $0.625 \leqslant x/D \leqslant 3$ through a pointwise comparison of each variable at subsequently decreasing tolerances. L_2 error norms for u, v, p, k and ε are analysed for each to assess the effect of the tolerance on the solution. In reality, the iterative and grid errors are not likely to be mutually exclusive. However, first reducing the iterative error substantially and then running finer grids with very high iterative tolerances minimizes the effect of iteration.

Grid independence is then tested by sequentially doubling the total number of elements in the domain to obtain three meshes with which the error norms are decreasing and an order of accuracy can be estimated. Note that, for the total number of elements to be doubled, the number of elements on one side of the mesh is increased by a grid refinement factor, $r = \sqrt{2}$ [1].

The procedure used here is taken primarily from References [1, 2]. First, absolute local errors, ϕ, are computed at all points, x of interest as $\phi(x) = X_c - X_f$, where X is a specific degree of freedom, the subscript f represents the fine grid, and the subscript c represents the next coarser grid. L_2 relative error norms are then computed as

$$\|X_f\|_2 = \frac{\sqrt{\sum_x [\phi(x)]^2}}{\max X_f} \tag{9}$$

Summation is taken at the same 100 points where iterative convergence was tested. These error norms are *not* used directly for determining grid independence via Richardson extrapolation. They can be employed for deriving a global order of accuracy for the model and for testing for global non-monotonicity.

It is sensible to check for non-monotonic convergence prior to computing the grid convergence index (GCI) to ensure that errors are decreasing in a consistent manner. If grid convergence is not monotonic, then a GCI cannot be computed. Non-monotonicity is tested by the convergence ratio, given by Stern *et al.* [1] based on a global L_2 norm as

$$R = \frac{\|X_f\|_2}{\|X_m\|_2} \tag{10a}$$

The local convergence ratio can also be calculated at any sampling point using the absolute error

$$R(x) = \frac{\phi_f(x)}{\phi_m(x)} \tag{10b}$$

Here, the subscript m refers to the refinement from the coarse to the medium mesh, and the subscript f refers to the refinement from the medium to the fine mesh. Notice that non-monotonicity cannot be tested without running the simulation on three successively finer grids. According to Stern *et al.* [1], monotonic convergence occurs when $0 < R < 1$. When $R < 0$, oscillatory convergence exists. The simulation is divergent when $R > 1$. However, Coleman *et al.* [42] demonstrate that oscillatory convergence can sometimes yield $0 < R < 1$. Thus, this test can only confirm if a simulation is not converging monotonically. The local convergence ratio is useful for determining specific points where the solution is divergent; hence, it is possible that a GCI can be computed for some but not all points.

The observed order of convergence must be computed prior to determining grid independence. It can also be computed from global or local errors. The global order of convergence is computed from the L_2 norms as [1]

$$p = \frac{\ln(\|X_m\|_2/\|X_f\|_2)}{\ln(r)} \tag{11a}$$

and the local order of convergence is [43]:

$$p(x) = \frac{\ln(\phi_m/\phi_f)}{\ln(r)} \tag{11b}$$

In the case where the local $p(x)$ is computed at each point, the overall order of convergence for each degree of freedom is given as the average of all points not shown to be divergent with respect to the convergence ratio. Advantages of local vs global computation of p will be addressed in the Results and Discussion section.

The GCI is used for δ_M in this study. The GCI is an error estimator based on Richardson extrapolation, which accounts for the order of accuracy of the simulation and the grid refinement factor chosen by the modeller, as well as for the error difference from one grid refinement to the next. The absolute GCI is computed at each sampling point as [2]

$$\mathrm{GCI}(x) = F_S \frac{\phi_f}{(r^p - 1)} \tag{12}$$

With the factor of safety, $F_S = 1$, the GCI reduces to the Richardson error estimator; F_S adds conservatism to the error estimate. A minimum $F_S = 1.25$ is recommended by Roache [2] when three grids have been studied to estimate the order of convergence. As noted before,

the GCI cannot be computed where the solution is known to be divergent. For this reason, use of a global convergence ratio in lieu of pointwise values may mislead the modeller to believe that the simulation is convergent everywhere when, in fact, oscillating or divergent conditions occur in some locations.

Because the simulations presented here are steady state, $\delta_T = 0$. Other contributions to the error can include stability enhancement techniques such as upwinding to minimize artificial viscosity and truncation of the eddy-viscosity and pressure terms [34]. δ_P is much more difficult to quantify because small changes in these parameters can either cause negligible or drastic effects, depending on their value prior to the change. For this reason, these parameters have been chosen using the guidelines of the software manufacturer to minimize their contribution to the numerical simulation error [28]. The overall error, δ_{SN}, is used to bound the computed values of u, v, p, k and ε when comparing the simulation results with experimental data.

EXPERIMENTAL METHODS

Wind tunnel

Experiments were performed in a recirculating wind tunnel located at the U.S. Environmental Protection Agency's Atmospheric Methods and Monitoring Branch (Research Triangle Park, NC). The tunnel consists of a blower powered by a 50-hp motor that draws air through a set of louvers. As the air passes the corner opposite to the blower, a set of direction vanes guides the air through a turbulence grid with $4'' \times 4''$ openings. After passing through a contraction, the air encounters a honeycomb grid, which removes any large-scale turbulent structures from the flow. Finally, the air travels downstream to the $1.52\,\text{m} \times 1.21\,\text{m} \times 7.30\,\text{m}$ test section where velocity measurements are taken with a two-dimensional 514-nm Argon-Ion laser phase Doppler anemometer (PDA) (Dantec Measurement Technology, Inc., Copenhagen, Denmark), which is described in detail in many publications including [44–47].

Tunnel speeds can reach up to 6.67 m/s. For a freestream velocity of 1.0 m/s, the tunnel velocity profile is uniform over the cross-section with a spatial coefficient of variation of 3.0%; the turbulence intensity at this speed is 3.5%. A detailed description of this tunnel can be found in Reference [47].

Measurements taken

Experiments at $Re = 5232$ are performed at a velocity of 1 m/s past a 0.0762 m diameter, 1.17 m tall smooth circular cylinder. The presence of the aluminum cylinder results in 4.8% blockage over the tunnel cross-sectional area. To detect the air motion, propylene glycol smoke particles are released into the air by a theatrical smoke generator (Martin Magnum Pro 2000, Århus, Denmark).

Two-dimensional air velocity is measured with the PDA at 140 positions downstream of the cylinder. Axi-symmetry is assumed so that measurement is made on only one side of the cylinder. Preliminary spot checking of the symmetry with the cylinder in place supports this assumption. This assumption is also supported by Heist *et al.* [47], which demonstrated that the velocity profile was nearly constant (with a coefficient of variation of 3%) over the cross-sectional height of the empty wind tunnel. The same wind tunnel is used in this

study. Measurements are made at only one height, 0.61 m above the floor and are taken at $0.625 \leqslant x/D \leqslant 4$ and $0 \leqslant y/D \leqslant 0.75$ with the origin located at the cylinder centre. Measuring points are spaced 0.125 diameters apart to obtain a detailed picture of the recirculation bubble downstream of the cylinder. A beam power of 3 W is maintained to eliminate noise from small particles [48, 49], and velocities from particles yielding a signal-to-noise ratio less than +1 dB are omitted to avoid bias in the velocity calculation [50].

From the time series of data collected at each measurement point, information about velocity and turbulence intensity is calculated; 95% confidence intervals for the velocity are computed based on measurement uncertainty resulting from signal noise and sampling independence. Details of each computation are given in Reference [51] for S/N and in Reference [52] for sample independence. Measurement uncertainty based on signal noise and sample independence is relatively low, $\sim O(10^{-3})$. Based on the optical constraints, limit of detection should not be an issue provided that the photodetectors are aligned for the optimal scattering angle of the seed particles, because laser Doppler anemometry is a primary standard measurement. However, data is subject to machine round-off error in signal processing. For the 8-bit signal processor, the round-off error results in computation to three significant digits. Hence, a limit of detection is estimated to be 0.001 m/s.

RESULTS AND DISCUSSION

Preliminary studies with the RNG k–ε/Speziale model demonstrate extremely slow iterative convergence. For this reason, we analyse the velocity field and the y^+ profile around the cylinder to ensure that we are obtaining a 'physical' result. It is found that the y^+ profile for the RNG k–ε/Speziale model is much different from the y^+ profile for the other models, which are similar to Figure 2. For the RNG k–ε/Speziale model, y^+ is very close to zero over the first 54° on the upstream side of the cylinder. A peak in y^+ at 104° corresponds to an isolated, sharp peak in the kinetic energy profile around the circular cylinder, which is also near zero around the upstream stagnation point. Because this finding is unphysical and apparently inhibits iterative convergence, the RNG k–ε/Speziale model is not included in the verification study.

Verification

Iterative convergence. Results from the iterative convergence test are shown in Table I for the standard k–ε and RNG k–ε models with a Boussinesq constitutive relationship and the RNG k–ε with a Launder constitutive relationship. The table displays relative L_2 error norms in u, v, p, k and ε for each order of magnitude change in iteration tolerance. For the standard k–ε and RNG k–ε/Boussinesq models, iterative convergence is achieved with errors that are $O(10^{-2})$ when changing the tolerance from 10^{-3} to 10^{-4}. While this error is reasonably low, decreasing the iteration tolerance two orders of magnitude to 10^{-6} yields all errors below 0.01 for the standard k–ε and RNG k–ε/Boussinesq model.

For the RNG k–ε with a Launder constitutive relationship, iterative convergence beyond a tolerance of 10^{-3} is not obtained. The pressure error stabilizes around 10^{-3} and does not show any sign of decreasing, although the other degrees of freedom had errors between 10^{-5} and 10^{-4}. To attain convergence to a tolerance of 10^{-3} for pressure in the RNG k–ε/

Table I. Two-norm errors resulting from changing the solution error tolerance for each model.

Solution error tolerance	u	v	k	ε
	Standard k–ε			
10^{-3}–10^{-4}	0.14	0.025	0.0094	0.0087
10^{-4}–10^{-5}	0.051	0.0099	0.0054	0.0038
10^{-5}–10^{-6}	0.0081	0.0014	0.00092	0.00062
	RNG k–ε/Boussinesq			
10^{-3}–10^{-4}	0.14	0.031	0.0056	0.0085
10^{-4}–10^{-5}	0.091	0.021	0.0087	0.0067
10^{-5}–10^{-6}	0.0077	0.0014	0.00085	0.00055
	RNG k–ε/Launder			
10^{-2}–10^{-3}			0.035	0.035
	0.29	0.093		

Launder model, the pressure clipping factor, used in FIDAP to clip small pivots in the matrix decomposition scheme [28], is decreased from 10^{-6} for the Boussinesq runs to 10^{-13}. To assess the iterative error for the RNG k–ε/Launder model, the L_2 error norm is compared for reducing the tolerance from 10^{-2} to 10^{-3}. These errors are $O(10^{-1})$. This is excessive, and the RNG k–ε/Launder model cannot be compared with experimental data. However, the Launder model is included in the grid independence portion of the verification study to illustrate the potential effect of large iterative errors on attaining grid independence.

Grid independence. For the standard k–ε model grid independence test, the mesh length scale is decreased by a factor of $\sqrt{2}$ to obtain a doubling of the number of elements in the domain outside the boundary layer. Table II shows the relative L_2 global error differences in u, v, k and ε for two mesh refinements from 38,642 ($M1$) to 78,242 ($M2$) elements and from 78,242 ($M2$) to 152,546 ($M3$) elements. Error differences decrease consistently over the two refinements. The global convergence ratio, R, is on average, 0.84. This result suggests that monotonicity cannot be ruled out for the standard k–ε method. The global order of accuracy, p, for the standard k–ε model is computed as 0.52 [1, 2]; the solution method is reported to be second-order accurate [28].

With second-order upwinding used for the convective terms, it would be expected that the overall $p \approx 2$. For this reason, local convergence ratios and orders of accuracy were computed for the standard k–ε method at each point, following Cadafalch *et al.* [43]. It was found that 19% of the sampling points had not reached the asymptotic limit of convergence for all degrees of freedom, where $0 < R < 1$, despite the global convergence ratio's indication of monotonicity. Hence, the global convergence ratios are misleading. When the divergent points are removed, $\bar{p} = 1.41$ for all degrees of freedom; this is much closer to the expected order of accuracy. However, $\bar{p}$ falls below the expected range for the u velocity with $\bar{p} = 0.84$. Further review of the data for u shows that only 20% of points have orders of accuracy in the expected range, with $\bar{p} = 1.27$. Only these locations can actually be considered verified with respect to the design of the method and used in validation of the u velocity field.

Table II. Global relative two-norm errors resulting from changing the mesh density for each mesh.

	u	v	k	ε
		Standard k–ε		
$M1$–$M2$	0.081	0.00891	0.0052	0.0050
$M2$–$M3$	0.064	0.0080	0.0042	0.0042
R	0.79	0.90	0.81	0.84
		RNG k–ε/Boussinesq		
$M1$–$M2$	0.092	0.010	0.0048	0.0055
$M2$–$M3$	0.070	0.0086	0.0038	0.0044
R	0.76	0.84	0.79	0.80
		RNG k–ε/Launder		
$M1$–$M2$	0.11	0.060	0.033	0.052
$M2$–$M3$	0.017	0.0099	0.0083	0.0090
$M3$–$M4$	0.29	0.10	0.12	0.12
$R(1-3)$	0.16	0.17	0.25	0.17
$R(2-4)$	17.02	10.48	14.27	13.48

$M1$: 38,642 elements; $M2$: 78,242 elements; $M3$: 152,546 elements; $M4$: 310,082 elements. Taken over the domain $0 \leqslant x/D \leqslant 3$, $0 \leqslant y/D \leqslant 0.5$. R is reported for the global convergence ratio.

Local GCIs are computed at non-divergent points where $1 < p < 2$ and displayed for u in Table III. The maximum GCI for u at non-divergent locations is 0.039; note that this is lower than the computed global L_2 norms, even with the factor of safety, order of accuracy and grid refinement factor taken into account. Factoring divergent points into the global norms causes an increase in the error. More refinement may need to be performed to achieve convergence at all locations; however, those exhibiting convergence can be used for comparison with experimental data.

It is unknown how many refinements are necessary for the solution to reach convergence at all points. Those points shown to converge can be considered in an asymptotic range. The GCI can then be used to extrapolate how many refinements are necessary to achieve convergence within 1% by [2]:

$$\mathrm{GCI_f} = \frac{\mathrm{GCI_c}}{r^p} \tag{13}$$

Using this technique, it can be shown that 2.44×10^6 grid points are necessary with the order of accuracy $p = 1.27$ to attain a GCI $< 1\%$ for points believed to be convergent.

Grid independence testing is performed for the RNG k–ε/Boussinesq model in the same manner as for the standard k–ε method. Again, global L_2 error differences are displayed in Table II. Global error differences decrease consistently over the two refinements. In this case, the global convergence ratio, $R = 0.80$, also suggests monotonic convergence. However, as for the standard $k \sim \varepsilon$, the global order of accuracy, 0.66, is well below the expected second-order accuracy of the method. Local tests for monotonicity demonstrate that 14% of the sampling points are divergent. When these points are removed, $\bar{p} = 1.27$ for all degrees of freedom; this order of accuracy is within the bounds of the method [43].

Table III. Local orders of accuracy and grid convergence indices for the u degree of freedom. Data are shown for the standard and RNG k–ε methods with Boussinesq constitutive relationships at locations where monotonic convergence is indicated and $1 < p < 2$.

Standard k–ε				RNG k–ε/Boussinesq			
x	y	p	GCI	x	y	p	GCI
0.375	0.375	1.21	0.0057	0.375	0.375	1.13	0.0052
0.5	0.375	1.45	0.012	0.5	0.375	1.50	0.0099
0.625	0.125	1.52	0.00031	0.625	0.125	1.029	0.00012
0.875	0.25	1.06	0.0090	0.875	0.25	1.18	0.0070
1	0.125	1.40	0.0020	1.375	0	1.39	0.0032
1.125	0	1.23	0.0022	1.5	0	1.072	0.0064
1.125	0.125	1.94	0.0028	1.5	0.25	1.33	0.017
1.375	0.5	1.01	0.039	1.875	0.5	1.029	0.041
1.5	0.125	1.54	0.0077	2.125	0.5	1.62	0.023
1.5	0.25	1.13	0.020	2.25	0.25	1.53	0.021
1.875	0.5	1.01	0.036	2.25	0.375	1.06	0.038
2.125	0.5	1.51	0.022	2.375	0.125	1.34	0.019
2.25	0.25	1.34	0.021	2.375	0.5	1.14	0.033
2.25	0.375	1.02	0.033	2.5	0.125	1.09	0.023
2.375	0.125	1.06	0.023	2.5	0.5	1.17	0.027
2.375	0.5	1.08	0.031	2.625	0.375	1.031	0.037
2.5	0.5	1.09	0.027	2.625	0.5	1.097	0.028
2.625	0.5	1.02	0.029	2.75	0.5	1.24	0.028
2.75	0.5	1.09	0.029	2.875	0.25	1.31	0.025
2.875	0.25	1.12	0.025	2.875	0.5	2.00	0.014
2.875	0.5	1.64	0.017	3	0.25	1.82	0.018
3	0.25	1.60	0.018				

Considering only the u degree of freedom, however, $\bar{p} = 1.01$. This is marginally acceptable within the limitations of the modeling technique [43].

Similar to the standard k–ε method, only 19% of points fall within the method's order of accuracy for u and should be used for comparison with experimental data. For these points, the average order of accuracy increases to $\bar{p} = 1.29$. The GCIs for u at locations where $1 < p < 2$ are displayed in Table III. The maximum error is 0.041, which is slightly greater than half of the global error in u for the RNG k–ε/Boussinesq method. Extrapolation using equation (13) demonstrates that 1.95×10^7 nodes are needed to attain an error $< 1\%$ for convergent locations with p=1.29. It is unknown how many cells are needed to attain convergence at all sampling points.

Table II also shows the absolute L_2 error differences in u, v, p, k, and ε for the RNG k–ε/Launder model. Errors decrease over the first two refinements for all degrees of freedom. Global R varies considerably for $M1 - M3$ for each degree of freedom, from 0.16 to 0.25. The corresponding computed global order of accuracy ranges from 3.95 to 5.28. For each degree of freedom, the global order of accuracy is much higher than expected for the method. For this reason, a fourth refinement to 310,082 ($M4$) elements is performed to determine whether the first three meshes represent a global grid independent solution. As shown in Table II, the L_2 error differences actually increase substantially over this refinement, over

100% for v and ε. $R > 1$ for each degree of freedom; global divergence is demonstrated. This establishes that, although the error decreases over three refinements, grid independence has not been achieved. Whether this error is due to the constitutive relationship or the high iterative error tolerance cannot be distinguished.

Experimental data comparison

Table IV compares recirculation zone lengths, interpolated from the velocity field, and separation angles found from the simulations and experiments. It is clear that both simulations greatly underestimate the length and width of the near wake. The separation points yielded by both models are closer to super-critical turbulent separation [53] than to that of sub-critical flow (e.g. Reference [54]). These observations agree with those of Rodi [7], Bosch and Rodi [8] and Kim and Boysan [10], where excessive production of turbulence kinetic energy upstream of the bluff body caused late separation and subsequent suppression of the near wake. Validation cannot be made for either model. However, to illustrate the verification process, u velocities are compared with experimental data in Figure 3 along $y/D = 0.5$, where many of the non-divergent points lie. The *GCI*s are used to develop error bars around the model values for the standard and RNG k–ε simulations, and only non-divergent locations

Table IV. Wake characteristics for each simulation and the experiment.

	Experiment	Standard k–ε	RNG k–ε/Boussinesq
Bubble length	2.15	1.51	1.81
Separation angle	83°	132°	131°

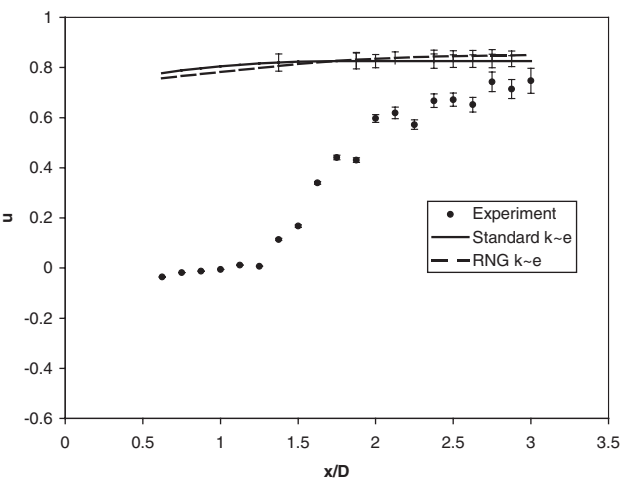

Figure 3. Comparison between standard k–ε and RNG k–ε/Boussinesq models and experimental data for the velocity profile at $y/D = 0.5$. Monotonic convergence is indicated by the error bars at all points displayed.

with acceptable orders of accuracy are used in the data comparison. As expected, no validation within the accuracy of the model is made. In this figure, it is evident that the model overestimates the near-wake velocity profiles.

CONCLUDING REMARKS

This work provides a verification study of RANS methods for the problem of airflow past a circular cylinder. It contributes an example of following a prescribed methodology for determining the accuracy of a CFD simulation [1, 2]. While most CFD studies presented in the literature do use multiple meshes, very few actually test for non-monotonic behaviour and compute the observed order of accuracy and GCIs. This study serves to demonstrate that these metrics are critical to understanding the limitations of a given simulation. For example, it would have been easy to conclude from the global convergence ratios that the standard and RNG k–ε simulations represented grid-independent solutions with which we could compare our experimental data. However, further study of the local GCIs demonstrated this to be untrue for the entire mesh and that $O(10^6-10^7)$ nodes would be required at minimum to achieve convergence at all pointwise locations. This clearly illustrates the issues involved when attempting to obtain accurate and reliable CFD results.

For the points where convergence was indicated, these predictions would be classified by Lasher [22] as category III. Qualitatively, the nature of flow past a two-dimensional circular cylinder was captured, despite notable differences between the simulation and experiment with respect to bubble length and separation point location. If the velocity field overprediction were maintained with changes in geometry or initial conditions, the models could be considered to provide category II predictions. While their value is somewhat limited for fluid dynamicists, engineers may perhaps derive some utility from the application.

ACKNOWLEDGEMENTS

The author wishes to thank Dr. Michael R. Flynn for many helpful discussions on this work. This article was supported in part by grant 1 R01 OH07363 from the National Institute for Occupational Safety and Health (NIOSH), Centers for Disease Control (CDC). Its contents are solely the responsibility of the authors and do not necessarily represent the official views of NIOSH. Computational resources were made available by the North Carolina Supercomputing Center, project 11059.

REFERENCES

1. Stern F, Wilson RV, Coleman HW, Paterson EG. Comprehensive approach to verification and validation of CFD simulations—Part 1: methodology and procedures. *Journal of Fluids Engineering* 2001; **123**:793–802.
2. Roache PJ. *Verification and Validation in Computational Science and Engineering.* Hermosa Publishers: Albuquerque, NM, 1998.
3. American Institute of Aeronautics and Astronautics. Guide for the verification and validation of computational fluid dynamics simulations. *AIAA-G-077-1998*. Washington, DC, 1998.
4. Lübcke H, Schmidt S, Rung T, Thiele F. Comparison of LES and RANS in bluff body flows. *Journal of Wind Engineering and Industrial Aerodynamics* 2001; **89**:1471–1485.
5. Breuer M. Large eddy simulation of the subcritical flow past a circular cylinder: numerical and modeling aspects. *International Journal for Numerical Methods in Fluids* 1998; **28**:1281–1302.
6. Majumdar S, Rodi W. Numerical calculations of turbulent flow past circular cylinders. *Third Symposium on Numerical and Physical Aspects of Aerodynamic Flow.* Long Beach, CA, 21–24 January 1985.

7. Rodi W. Comparison of LES and RANS calculations of the flow around bluff bodies. *Journal of Wind Engineering and Industrial Aerodynamics* 1997; **69–71**:55–75.
8. Bosch G, Rodi W. Simulation of vortex shedding past a square cylinder near a wall. *International Journal of Heat and Fluid Flow* 1996; **17**:267–275.
9. Bosch G, Rodi W. Simulation of vortex shedding past a square cylinder with different turbulence models. *International Journal for Numerical Methods in Fluids* 1998; **28**:601–616.
10. Kim S-E, Boysan F. Application of CFD to environmental flows. *Journal of Wind Engineering and Industrial Aerodynamics* 1999; **81**:145–158.
11. Chen Y-S, Kim S-W. Computation of turbulent flows using an extended k–ε turbulence closure model. NASA-CR-179204, 1987.
12. Jenne M, Reuss M. A critical assessment on the use of the k–ε turbulence models for simulation of the turbulent liquid flow induced by a rushton-turbine in baffled stirred-tank reactors. *Chemical Engineering Science* 1999; **54**:3921–3941.
13. Henkes RAWM. Scaling of the turbulent boundary layer along a flat plate according to different turbulence models. *International Journal of Heat and Fluid Flow* 1998; **18**:338–347.
14. Shih T-H, Liou WW, Shabbir A, Yang Z, Zhu J. A new k–ε viscosity model for high Reynolds number turbulent flows. *Computers and Fluids* 1995; **24**:227–238.
15. Lumley JL. Some comments on turbulence. *Physics of Fluids A* 1992; **4**:203–211.
16. Yakhot V, Orszag SA. Renormalization group analysis of turbulence. *Journal of Scientific Computing* 1986;**1**:3.
17. Franke R, Rodi W, Shönung B. Analysis of experimental vortex-shedding data with respect to turbulence modelling. *Seventh Symposium on Turbulent Shear Flows*, Stanford University, 21–23 August 1989.
18. Mompean G, Gavrilakis S, Machiels L, Deville MO. On predicting the turbulence-induced secondary flows using nonlinear k–ε models. *Physics of Fluids* 1996; **8**:1856–1868.
19. Jeong UY, Koh H-M, Lee HS. Finite element formulation for the analysis of turbulent wind flow passing bluff structures using the RNG k–ε method. *Journal of Wind Engineering and Industrial Aerodynamics* 2002; **90**: 151–169.
20. Chang K-A, Hsu T-J, Liu PL-F. Vortex generation and evolution in water waves propagating over a submerged rectangular obstacle. *Coastal Engineering* 2001; **44**:13–36.
21. Bojic M, Lee M, Yik F. Flow and temperatures outside a high-rise residential building due to heat rejection by its air conditioners. *Energy and Buildings* 2001; **33**:737–751.
22. Lasher WC. Computation of two-dimensional blocked flow normal to a flat plate. *Journal of Wind Engineering and Industrial Aerodynamics* 2001; **89**:493–513.
23. Bradshaw P. Understanding and prediction of turbulent flow—1996. *International Journal of Heat and Fluid Flow* 1997; **18**:45–54.
24. Launder BE, Sharma BI. Application of the energy dissipation model of turbulence to the calculation of flow near a spinning disk. *Letters of Heat and Mass Transfer* 1974; **1**:131.
25. Schmidt S, Thiele F. Comparison of numerical methods applied to the flow over wall-mounted cubes. *International Journal of Heat and Fluid Flow* 2002; **23**:330–339.
26. Spalart PR. Strategies for turbulence modelling and simulations. *International Journal of Heat and Fluid Flow* 2000; **21**:252–263.
27. van Dam CP. Recent experiences with different methods of drag prediction. *Progress in Aerospace Science* 1999; **35**:751–798.
28. Fluent, Inc. *FIDAP User's Manual*, *Version 8.* Fluent, Inc.: Evanston, IL, 1999.
29. Hughes TJR, Brooks AN. A multidimensional upwind scheme with no cross-wind diffusion. In *Finite Element Methods for Advection Dominated Flows*, TJR Hughes (ed.). ASME Publication ASME-AMD: New York, 1979; 34.
30. Celik I, Shaffer FD. Long time-averaged solutions of turbulent flow past a circular cylinder. *Journal of Wind Engineering and Industrial Aerodynamics* 1995; **56**:185–212.
31. Wilcox DC. Simulation of transition with a two-equation turbulence model. *AIAA Journal* 1994; **32**:247–255.
32. Launder BE, Spalding DB. The numerical computation of turbulent flows. *Computer Methods in Applied Mechanics and Engineering* 1974; **3**:269–289.
33. Bosch G. Simulation der Turbulenten Umströmung eines Quadratischen Zylinders bei $Re = 22,000$. *Report SFB* 210/T/103. Universität Karlsruhe: Karlsruhe, Germany, 1995.
34. Ignat L, Pelletier D, Illinca F. A universal formulation of two-equation models for adaptive computation of turbulent flows. *Computer Methods in Applied Mechanics and Engineering* 2000; **189**:1119–1139.
35. Speziale CG. On nonlinear K–l and K–ε models of turbulence. *Journal of Fluid Mechanics* 1987; **178**: 459–475.
36. Craft TJ, Launder BE, Suga K. Development and application of a cubic eddy-viscosity model of turbulence. *International Journal of Heat and Fluid Flow* 1996; **17**:108–115.

37. Launder BE, Morse A, Rodi W, Spalding DB. The prediction of free shear flows—a comparison of the performance of six turbulence models. *Proceedings of NASA Conference on Free Shear Flows*, Langley (Also *Imperial College Mechanical Engineering Department Report TM/TN/A/19*), 1972.
38. Yakhot V, Orszag SA, Thangam S, Gatski TB, Speziale CG. Development of turbulence models for shear flows by a double expansion technique. *Physics of Fluids A* 1992; **4**:1510–1520.
39. Smith LM, Reynolds WC. On the Yakhot–Orszag renormalization group method for deriving turbulence statistics and models. *Physics of Fluids A* 1992; **4**:364–390.
40. Reichardt H. Vollständige darstellung der turbulenten geschwindigkeitsverteilung in glatten leitungen. *Zeitschrift Angewandte Mathematik* 1951; **31**:208–219.
41. Launder BE. Numerical computation of convective heat transfer in complex turbulent flows: time to abandon wall functions? *International Journal of Heat and Mass Transfer* 1984; **27**:1485–1491.
42. Coleman HW, Stern F, Di Mascio A, Campana E. The problem with oscillatory behavior in grid convergence studies. *Journal of Fluids Engineering* 2001; **123**:438–439.
43. Cadafalch J, Pérez-Segarra CD, Còsul R, Oliva A. Verification of finite volume computations on steady-stae flow with corner singularities. *Journal of Fluids Engineering* 2002; **124**:11–21.
44. Durst F, Whitelaw JH. Optimization of optical anemometers. *Proceedings of the Royal Society of London A* 1971; **324**:157–181.
45. Foreman JW, George EW, Lewis RD. Measurement of localized flow velocities in gases with a laser doppler flowmeter. *Applied Physics Letters* 1969; **7**:77–78.
46. Rudd MJ. A new theoretical model for the laser Dopplermeter. *Journal of Scientific Instruments* 1969; **2**:55–58.
47. Heist DK, Richmond-Bryant J, Eisner A, Conner T. Development of a versatile aerosol generation system for use in a large wind tunnel. *Aerosol Science and Technology* 2003; **37**:293–301.
48. Drain LE. Coherent and noncoherent methods in doppler optical beat velocity measurement. *Journal of Physics D: Applied Physics* 1972; **5**:481–495.
49. Lading L. Analysis of signal-to-noise ratio of the laser Doppler velocimeter. *Opto-electronics* 1973; **5**:175–187.
50. Ibrahim KM, Werthimer GD, Bachalo WD. Signal processing considerations for laser Doppler and phase Doppler applications, *Applications of Laser Techniques to Fluid Mechanics*, *5th International Symposium*, Lisbon, Portugal, 1990.
51. Høst-Madsen A, Caspersen C. The limitations in high frequency turbulence spectrum estimation using the laser doppler anemometer. *Seventh International Symposium on Applications of Laser Techniques to Fluid Mechanics*, 1994.
52. Winter AR, Graham LJW, Bremhorst K. Velocity bias associated with laser Doppler anemometer controlled processors. *Journal of Fluids Engineering* 1991; **113**:250–255.
53. Song CCS, Yuan M. Simulation of vortex-shedding flow about a circular cylinder at high Reynolds numbers. *Journal of Fluids Engineering* 1990; **112**:155–161.
54. Cantwell B, Coles D. An experimental study of entrainment and transport in the turbulent wake of a circular cylinder. *Journal of Fluid Mechanics* 1983; **136**:321–374.

